An Experimental Evaluation of Endmember Generation Algorithms

Antonio Plaza, Juan J. Sánchez-Testal, Javier Plaza and David Valencia

Polytechnic Institute of Cáceres
Computer Science Department, University of Extremadura
Avda. de la Universidad s/n, E-10071 Cáceres, Spain
Phone: +34 927 257195 – Fax: +34 927 257203
Contact e-mail: aplaza@unex.es

ABSTRACT

Hyperspectral imagery is a new class of image data which is mainly used in remote sensing. It is characterized by a wealth of spatial and spectral information that can be used to improve detection and estimation accuracy in chemical and biological standoff detection applications. Finding spectral endmembers is a very important task in hyperspectral data exploitation. Over the last decade, several algorithms have been proposed to find spectral endmembers in hyperspectral data. Existing algorithms may be categorized into two different classes: 1) endmember extraction algorithms (EEAs), designed to find pure (or purest available) pixels, and 2) endmember generation algorithms (EGAs), designed to find pure spectral signatures. Such a distinction between an EEA and an EGA has never been made before in the literature. In this paper, we explore the concept of endmember generation as opposed to that of endmember extraction by describing our experience with two EGAs: the optical real-time adaptative spectral identification system (ORASIS), which generates endmembers based on spectral criteria, and the automated morphological endmember extraction (AMEE), which generates endmembers based on spatial/spectral criteria. The performance of these two algoriths is compared to that achieved by two standard algorithms which can perform both as EEAs and EGAs, i.e., the pixel purity index (PPI) and the iterative error analysis (IEA). Both the PPI and IEA may also be used to generate new signatures from existing pixel vectors in the input data, as opposed to the ORASIS method, which generates new spectra using an minimum volume transform. A standard algorithm which behaves as an EEA, i.e., the N-FINDR, is also used in the comparison for demonstration purposes. Experimental results provide several intriguing findings that may help hyperspectral data analysts in selection of algorithms for specific applications.

Keywords: Hyperspectral imaging, Endmember generation, Endmember extraction, Quantitative and comparative algorithm assessment, Spectral signature purity.

1. INTRODUCTION

An "endmember" in imaging spectroscopy-related studies can be defined as an idealized, pure spectral signature for a class[1]. This concept should be distinguished from the concept of "pure pixel" traditionally adopted in multispectral data analysis[2]. As opposed to that concept, the the term "pixel" in hyperspectral imaging generally refers to an L-dimensional vector given by hundreds of spectral values corresponding to different wavelengths[3]. It should be noted that an endmember is generally not a pixel. It is a spectral signature that is completely specified by the spectrum of a single material substance. Accordingly, a pixel can only be properly called "pure" if its spectral signature is an endmember. However, due to available spatial resolution and mixing phenomena, most remotely sensed hyperspectral data sets are dominated by mixed pixels, and such pure pixels may be very difficult to be found in real-world analysis scenarios.

Several algorithms have been proposed over the last decade with the purpose of finding endmembers directly from the image data[4]. Such image-derived endmembers present advantages over library and field spectra, which are not necessarily acquired under the same conditions as the airborne or satellite image data. Further, important surface components may not be adequately represented in such spectral libraries. Finally, image endmembers also have the advantage of being directly associated with surface components detectable in the scene. Spectral mixture analysis (SMA) involves the separation of a pixel spectrum into its component endmember spectra and the estimation of the abundance value for each endmember in the pixel[3]. However, if the image-derived endmembers are not carefully selected, such

Chemical and Biological Standoff Detection III, edited by James O. Jensen, Jean-Marc Thériault,
Proc. of SPIE Vol. 5995, 599501, (2005) · 0277-786X/05/$15 · doi: 10.1117/12.630778

inversion techniques may result in negative and/or unrealistic abundance fraction estimations. With the purpose of providing a snapshot of the current state-of-the-art in the area of endmember extraction, Table 1 provides an overview of the endmember finding algorithms that will be considered in this study where a clear distinction is made between those algorithms that belong to the "endmember extraction" (EEA) category, those in the "endmember generation" (EGA) category, and those that can be used as both EEA/EGAs depending on the application under study.

Method	Pixel Purity Index (PPI)	N-FINDR	Iterative Error Analysis (IEA)	ORASIS	Automated Morphological Endmember Extraction (AMEE)
Nature	Supervised	Automatic	Automatic	Automatic	Automatic
Algorithm assumptions	MNF-based reduction in the data	MNF-based reduction in the data	None	None	None
Dimension reduction	Yes	Yes	No	No	No
Convergence property	Maximum number of runs	Simplex with maximum volume	Minimum error in unmixings	All exemplar spectra found	Range of spatial kernels
Computational complexity	High number of skewer runs required	Depends on initial random selection	Significant due to repeated constrained unmixings	Algorithm tuned for very rapid execution	Depends on the range of spatial kernels used
Use of spatial information	No	No	No	No	Yes
EEA/EGA	Both	EEA	Both	EGA	EGA

Table 1. Summary of five selected endmember finding algorithms.

The distinction between an EEA and an EGA is crucial and has been rarely addressed before in the hyperspectral imaging literature. An EEA is generally designed to find pure pixels, i.e., it assumes that all the endmembers have pure pixel representation in the scene. However, it should be taken into account that the presence of pure class pixels in the image data largely depends on available sensor spatial resolution. As a result, there may be cases where it is not possible for a certain algorithm to find such pure pixels in a scene. In those cases, it is probable that the algorithm may generally find the set of *most highly pure pixels available in the data*, even though their signatures may not be completely pure. In such case, the fractional components found for the mixed pixels through SMA are usually expressed in terms of other mixed pixels (the endmembers identified by the algorithm) and not in terms of pure class signatures. To address this issue, an EGA is generally designed to find pure class signatures, which may not be real pixels represented in the image.

One of the most representative EGAs in recent years has been the Naval Research Laboratory's Optical Real-time Adaptive Spectral Identification System (ORASIS)[5] method. This method consists of several algorithms organized in six modules: exemplar selector, adaptive learner, demixer, knowledge base/spectral library, and spatial postprocessor. The first step consists in flat fielding the spectra. Next, the exemplar selection module is used to select pixel vectors that represent the smaller convex cone containing the data. The other pixel vectors are rejected when the spectral angle distance is less than a given threshold (the algorithm is sensitive to the threshold parameter). The procedure then finds the basis for a subspace of a lower dimension using a a Gram-Schmidt orthogonalization[5]. The selected vectors are then projected onto this subspace, and a simplex is found by a minimum volume transform algorithm (originally developed by Craig[6]) which constructs the simplex of minimum volume *enclosing* all the data. Therefore, ORASIS generates spectral signatures at the corners of the hypercube defined by the input data.

The main difference between ORASIS and Winter's N-FINDR[7], another highly representative algorithm of the EEA class, is the fact that the former uses a so-called *gift wrapping algorithm* that tries to find the simplex with maximum volume that can be inscribed in the data using *real pixels*. In other words, while the ORASIS seeks for the simplex with minimum volume that can enclose all the pixels in the input data (and without the need to use real pixel vectors to achieve such goal), the N-FINDR tries to inflate the simplex with maximum volume using real pixel vectors in the data. If no sufficiently *extreme* or *eccentric* pixels are present, then there may be a chance that several mixed pixels would fall outside of the simplex, thus introducing negative or unrealistic abundance fractions (at least, under the most common linear mixture analysis approach[8]). However, even though ORASIS may generate endmembers which can be used to describe other mixed pixels in the scene using *realistic* abundance fractions, there is a risk that the spectral signatures generated by ORASIS may in turn be *unrealistic* from a physical point of view.

In this paper, we explore the concept of endmember generation as opposed to that of endmember extraction by describing our experience with two EGAs, i.e., the ORASIS algorithm (which generates endmembers from a spectral

point of view) and the Automated Morphological Endmember Extraction (AMEE)[9] algorithm (which generates endmembers from a spatial/spectral point of view). Two well-known algorithms that can act both as EEAs and EGAs, i.e., Boardman et al.'s Pixel Purity Index (PPI)[10] and Iterative Error Analysis (IEA)[11], are also included in the comparison. In both cases, the procedure used to generate endmembers is similar to that used by the AMEE, i.e., they use real pixel vectors to generate new signatures using statistical procedures. Finally, a highly representative algorithm of the EEA class such as the N-FINDR algorithm is also evaluated.

The remainder of the paper is organized as follows. Section 2 provides an overview of the algorithms that will be compared in this study. Section 3 describes the image data used for evaluation purposes, collected by the NASA's Jet Propulsion Laboratory's Airborne Visible Infra-Red Imaging Spectrometer (AVIRIS)[12] over the Jasper Ridge Biological Preserve in California. Section 4 describes our experimental assessment of EGAs and EEAs, and discusses on the appropriate use of the two types of algorithms in the application under study using diffferent criteria. Finally, section 5 concludes with some remarks and hints at plausible future research.

2. ALGORITHMS

This section develops first describes two EGAs, i.e., the ORASIS and AMEE algorithms. Then, the N-FINDR algorithm is presented as a representative case of EEA for experiments in this paper. Finally, algorithmic descriptions of PPI and IEA algorithms (which can be used as both EGAs and EEAs) are also provided. It should be noted that most of the algorithmic descriptions provided below correspond to our implementation and understanding of the algorithms, except for the case of ORASIS, where the final results where directly provided by the algorithm's developers at NRL and we only implemented the exemplar selector module. Nevertheless, our experiments with such module also provided some interesting findings that will be addressed in section 4.

2.1. ORASIS algorithm

The first step applied by the method is a preprocessing, which consists of flat fielding and various tests on the spectra. Next, an exemplar selection process is run with the purpose of prescreening the data for unique spectra, thus creating a representative set of exemplar vectors that can be used as endmembers for spectral unmixing. This procedure rejects redundant spectra by calculating the spectral angle distance between spectral vectors. Any vector that is not separated by a certain threshold angle $t^{(\mathrm{ORASIS})}$ is removed from the data. The procedure then finds a basis set of much lower dimension than the original data by a modified Gram–Schmidt process[5]. The exemplar spectra are then projected onto this basis subspace, and a simplex is found through a minimum volume transform. The exemplar selector module, whose goal is to reduce the volume of data with minimal loss of important information, can be seen as a single-pass learning vector quantization (LVQ) process. In this regard, the exemplars are representative of the entire dataset, i.e., all spectra in the original data are within $t^{(\mathrm{ORASIS})}$ spectral angle of at least one exemplar. This is a quantization aspect of the screener that will be thoroughly analyzed in experiments, along with the capacity of the algorithm to generate *realistic* spectral signatures in the context of specific applications.

2.2. AMEE algorithm

The AMEE algorithm is the only method discussed in this paper that makes simultaneous use of spatial and spectral information via multi-channel morphological processing[13,14]. Let $\boldsymbol{f}$ denote the input data cube and $\boldsymbol{f}(x,y)$ denote the pixel vector at spatial location (x,y). Similarly, let K be a kernel defined in the spatial domain of the image (the x-y plane). This kernel is translated over the image and acts as a probe for extracting or suppressing specific structures of the image objects, according to its size and shape. The AMEE method is based on the application of multi-channel erosion and dilation operations to the data, which are respectively defined as follows.

$$(\boldsymbol{f} \otimes \mathrm{K})(\mathrm{x},\mathrm{y}) = \arg\_\ \mathrm{Min}_{(\mathrm{s},\mathrm{t})\in \mathrm{K}} \left\{ \sum_{\mathrm{s}} \sum_{\mathrm{t}} \mathrm{SAM}\left(\boldsymbol{f}(\mathrm{x},\mathrm{y}), \boldsymbol{f}(\mathrm{x}+\mathrm{s},\mathrm{y}+\mathrm{t})\right) \right\} \tag{1}$$

$$(\boldsymbol{f} \oplus \mathrm{K})(\mathrm{x},\mathrm{y}) = \arg\_\ \mathrm{Max}_{(\mathrm{s},\mathrm{t})\in \mathrm{K}} \left\{ \sum_{\mathrm{s}} \sum_{\mathrm{t}} \mathrm{SAM}\left(\boldsymbol{f}(\mathrm{x},\mathrm{y}), \boldsymbol{f}(\mathrm{x}-\mathrm{s},\mathrm{y}-\mathrm{t})\right) \right\} \tag{2}$$

where SAM is the spectral angle mapper[3]. Multi-channel erosion extracts the pixel vector that is more similar to its neighbors as opposed to multi-channel dilation, which extracts the most spectrally distinct pixel in the neighborhood (endmember candidate). A morphological eccentricity index (MEI)[9] is defined for each endmember candidate by calculating the spectral angle between the pixel provided by the dilation operation and the pixel provided by the erosion. This operation is repeated for all the pixels in the scene, using kernels with a range of different sizes, until a final MEI image is generated. Automated endmember selection is performed from the MEI image obtained in the competitive endmember selection step by a threshold value which is automatically calculated using the multi-level Otsu method, an approach based on the minimization of the weighted sum of group variances[9]. The final selection is refined by a region-growing procedure that incorporates neighboring pixels that are sufficiently similar (according to a certain threshold angle parameter $t^{(\mathrm{AMEE})}$) to the regions obtained after thresholding. Mean spectra are obtained for the resulting regions after the region-growing process. As a consequence, a final set of p endmembers is generated by the algorithm according to spatial/spectral criteria.

2.3. N-FINDR algorithm

The N-FINDR algorithm developed by Winter et al. [7] assumes that, in L spectral dimensions, an L-volume formed by a simplex with vertices specified by purest pixels is always larger than that formed by any other combination of pixels. The algorithm is initialized by a simplex within the data whose vertices are formed by a random set of pixels, $\left\{\mathbf{e}_1^{(0)}, \mathbf{e}_2^{(0)}, \Lambda, \mathbf{e}_p^{(0)}\right\}$ where p is the number of endmembers required to be extracted. It then finds $V(\mathbf{e}_1^{(0)}, \mathbf{e}_2^{(0)}, \Lambda, \mathbf{e}_p^{(0)})$, the volume of the simplex with vertices $\mathbf{e}_1^{(0)}, \mathbf{e}_2^{(0)}, \Lambda, \mathbf{e}_p^{(0)}$, denoted by $S(\mathbf{e}_1^{(0)}, \mathbf{e}_2^{(0)}, \Lambda, \mathbf{e}_p^{(0)})$. Then, for each sample vector $\mathbf{x}$, it recalculates the volumes of p simplices, $S(\mathbf{x}, \mathbf{e}_2^{(0)}, \Lambda, \mathbf{e}_p^{(0)})$, $S(\mathbf{e}_1^{(0)}, \mathbf{x}, \Lambda, \mathbf{e}_p^{(0)})$, … , $S(\mathbf{e}_1^{(0)}, \mathbf{e}_2^{(0)}, \Lambda, \mathbf{x})$, each of which is formed by replacing one endmember $\mathbf{e}_j^{(0)}$ with the sample vector $\mathbf{x}$. If none of these p recalculated volumes is greater than $S(\mathbf{e}_1^{(0)}, \mathbf{e}_2^{(0)}, \Lambda, \mathbf{e}_p^{(0)})$, then no endmember in $\mathbf{e}_1^{(0)}, \mathbf{e}_2^{(0)}, \Lambda, \mathbf{e}_p^{(0)}$ will be replaced. Otherwise, the endmember which is absent in the largest volume among the p simplices, $S(\mathbf{x}, \mathbf{e}_2^{(0)}, \Lambda, \mathbf{e}_p^{(0)})$, $S(\mathbf{e}_1^{(0)}, \mathbf{x}, \Lambda, \mathbf{e}_p^{(0)})$, … , $S(\mathbf{e}_1^{(0)}, \mathbf{e}_2^{(0)}, \Lambda, \mathbf{x})$, will be replaced by the sample vector $\mathbf{x}$. Let such an endmember be denoted by $\mathbf{e}_j^{(0)}$. A new set of endmembers is produced by letting $\mathbf{e}_j^{(1)} = \mathbf{x}$ and $\mathbf{e}_i^{(1)} = \mathbf{e}_i^{(0)}$ for $i \neq j$. This process is repeated again until all the sample vectors are exhausted.

2.4. PPI algorithm

The PPI algorithm developed by Boardman et al.[10] is a simple technique that searches for a set of vertices of a convex hull of an L-dimensional data space. It is a very popular technique due to its availability in Kodak's Research Systems ENVI[15] software. The algorithm is initialized by a large set of randomly generated L-dimensional vectors called "skewers", denoted by $\{\mathbf{skewer}_j\}$. For each $\mathbf{skewer}_j$, all the data sample vectors are projected onto $\mathbf{skewer}_j$ to find sample vectors at its extreme positions to form an extrema set for the $\mathbf{skewer}_j$, denoted by $S_{extrema}(\mathbf{skewer}_j)$. Despite the fact that a different $\mathbf{skewer}_j$ generates a different extrema set $\mathrm{S}_{\mathrm{extrema}}(\mathbf{skewer}_j)$, it is very likely that some sample vectors may appear in more than one extrema set. If we define an indicator function of a set S by $I_S(\mathbf{x}) = \begin{cases} 1; \text{if } \mathbf{x} \in S \\ 0; \text{if } \mathbf{x} \notin S \end{cases}$, the PPI selects those sample vectors that yield $t^{(\mathrm{PPI})}$ largest values of $N_{PPI}(\mathbf{x}) = \sum_j I_{S_{extrema}(skewer_j)}(\mathbf{x})$. These pixels are then loaded in an L-dimensional visualization space and a subset of $p \leq t^{(\mathrm{PPI})}$ pixels falling in the corners of the data cube is manually selected by a trained user for endmember extraction. This is done through a companion tool available in ENVI software known as "L-dimensional visualizer"[15] which allows for the rotation and visualization of the L-dimensional data using projections until a set of spectrally extreme pixels can be visually identified and labeled. It is worth noting that such tool allows for the generation of final endmember spectra by selecting clusters of pixels in spectral space, in which case all the pixels which are labeled as being part of a certain pure class are averaged together to generate the spectral signature for a class. In such case, the final generated endmembers are not real pixels in the data. Of course, the tool also allows for the selection of individual extreme pixels in the data cloud. In this case, the algorithm behaves strictly as an EEA because the final selected pixels are actually real pixel vectors in the input data.

2.5. IEA algorithm

The IEA algorithm makes use of constrained linear spectral unmixing[8] to search for possible endmembers. In other words, a series of constrained unmixing operations is performed, each time selecting as endmembers the pixels that minimize the remaining error in the unmixed image. An initial vector (usually the mean spectrum of the data) is chosen to start the process. A constrained linear spectral unmixing in terms of this vector is performed, and an error image, formed by the errors remaining at each pixel after the unmixing operation, is calculated. The user then selects a desired number of endmembers, p, a number of pixels, R, and a spectral angle value, θ, where R is the number of pixels with the largest number of errors, selected from the error image. The spectral vector corresponding to the pixel with the single largest error is found. A subset of R consisting of all those pixels that fall within an angle θ of the maximum error vector is then calculated, and these pixels are averaged to produce the new endmember vector. This process iscontinued until p endmembers have been selected. By looking at the algorithm description above, we can notice that the endmembers produced by the IEA are the averaged values of a set of selected pixels, not true pixels in the data[11]. In order to make the algorithm behave as an EEA, we can set $R = 1$ and $\theta = 0$. In this case, the IEA-generated endmembers are actually real pixels in the data. There is also a salient different between IEA and all other endmember finding algorithms considered in this study. Other algorithms generally produce a set of p endmembers *simultaneously*. So, for a different value of p, an endmember finding algorithm must be re-implemented to produce a different set of p endmembers. In other words, for any given number of endmembers, the algorithm must re-search all the endmembers because the set of p-1 endmembers produced is not necessarily a subset of a set of p endmembers found by the same algorithm. As a result, most available algorithms cannot take advantage of its previously generated p-1 endmembers to be included as part of p endmembers. This limitation is not present in the IEA, which can behave as an iterative endmember extraction/generation algorithm in the sense that it produces the final set of endmebers *sequentially* in order. As a result, the set of p final IEA endmembers always includes the set of previously found p-1 endmembers.

3. HYPERSPECTRAL DATA DESCRIPTION

An AVIRIS imaging spectrometer dataset collected over the Jasper Ridge Biological Preserve (JRBP) in California have been selected for experiments [see Fig. 1(left)]. The data are available online (from http://aviris.jpl.nasa.gov) and consists of 512x614 pixels and 224 spectral bands, with a nominal ground resolution of 20 m, spectral resolution of 10 nm, and 16-bit radiometric resolution. In a previous study of surface materials over JRBP, reference spectral endmembers were derived from the scenes above based on extensive ground knowledge[16]. Fig. 1(right) plots spectral signatures associated to the main constituent materials at JRBP. These signatures, denoted from now on as $\boldsymbol{s}_1$ (soil), $\boldsymbol{s}_2$ (evergreen forest), $\boldsymbol{s}_3$ (dry grass), $\boldsymbol{s}_4$ (chaparral vegetation), and $\boldsymbol{s}_5$ (shade), were compiled by using a hybrid method that combines visual inspection and prior information about the scene. Specifically, ground knowledge was used to identify homogeneous vegetation, shadow and soil areas in the scene. Inside those areas, representative pixels were selected as ground-truth spectra by comparing them to a spectral library of field data[16], used to represent landscape components at JRBP. In this process, we ensured that library spectra matched the phenology at the time of the image, and that there was little or no miscalibration between field spectra and image spectra.

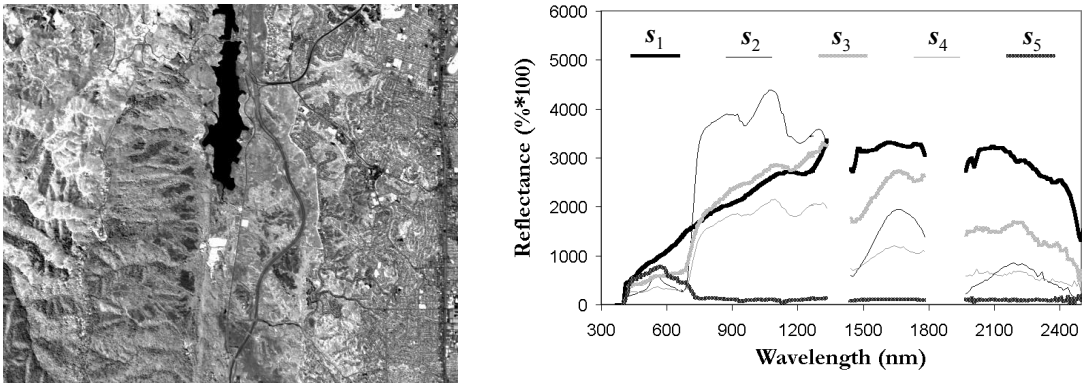

Figure 1. (Left) Spectral band at 903 nm of an AVIRIS hyperspectral image collected over the Jasper Ridge biological preserve in California. (Right) Ground-truth endmember signatures of soil, forest, dry grass, chaparral vegetation and shade, respectively.

4. EXPERIMENTAL RESULTS

A comparative study of ORASIS, AMEE, N-FINDR, PPI and IEA in the tast of extracting/generating endmembers from the JRBP hyperspectral data collected by AVIRIS is described in this section. In particular, we show a performance comparison of EEAs/EGAs in section 2 using selected image endmembers in Fig. 1(right) as ground-truth information. Before addressing the obtained results, we must point out that they were obtained using H-COMP[17], our custom-designed tool that incorporates several metrics for hyperspectral analysis. We also believe that comments about the SNR in the AVIRIS sensor at the time of data acquisition are pertinent. In this regard, it should be noted that the highest SNR levels calculated in 1998 for a 50% reflectance target at sea level and 23.5º zenith angle corresponds in the A spectrometer (0.7 μm) to levels of 1000:1 and the lowest were measured in the SWIR region (2.2 μm) with levels of 400:1[12]. These leves are even much higher now after several recent improvements to the AVIRIS sensor.

In order to ensure a fair comparison between the different methods tested, the best performance must be obtained from each alternative method. Then, prior to a full examination and discussion of results, it is important to outline parameter values used for ORASIS, AMEE, N-FINDR, PPI and IEA algorithms. In all cases, the number of endmembers to be found by the different methods was estimated using the virtual dimensionality (VD) concept[18]. Specifically, the method used to determine the VD in this paper is the one developed by Harsanyi-Farrand-Chang[3], referred to as HFC method, which calculates eigenvalues from both sample correlation matrix and sample covariance matrix, referred to as correlation-eigenvalues and covariance-eigenvalues for each of spectral bands. Consequently, if a distinct spectral signature generally makes a contribution to eigenvalue-represented signal energy in one spectral band, then its associated correlation-eigenvalue is greater than its corresponding covariance-eigenvalue in this particular band. Otherwise, the correlation-eigenvalue is equal to its corresponding covariance-eigenvalue, in which case only noise is present in this particular band. Using this concept, a binary composite hypothesis testing problem can be formulated with the null hypothesis representing the case that correlation-eigenvalue is equal to its corresponding covariance-eigenvalue and the alternative hypothesis corresponding to the case that the correlation-eigenvalue is greater than its corresponding covariance-eigenvalue. By specifying a false alarm probability, P_F, a Neyman-Pearson detector can be further derived to determine whether or not a distinct signature is present in each of spectral bands. Table 1 tabulates the estimated VD values for the AVIRIS JRBP scene using various false alarm probabilities. According to the table, an appropriate estimate seemed to be $p = 20$ for $P_F = 10^{-3}$, 10^{-4} and 10^{-5}.

$P_F = 10^{-1}$	$P_F = 10^{-1}$	$P_F = 10^{-1}$	$P_F = 10^{-1}$	$P_F = 10^{-1}$
34	26	20	20	20

Table 2. VD estimated by the HFC method for the AVIRIS scene in Fig. 1(a).

Although in practice it is very difficult to optimize every considered method for performance analysis, we have used our previous experience with the methods[4] to select parameters that are reasonably close to optimal for the test data. This was particularly an issue for the two methods that can be used as both EEAs and EGAs, i.e., the PPI and the IEA algorithms. For instance, we observed that PPI produced the same final set of endmembers when the value of was above 3000 iterations (values of 10^4, 10^5 and 10^6 iterations were tested). Based on the above simple experiment, the cutoff threshold $t^{(\mathrm{PPI})}$ was set to the mean of PPI scores obtained after 3000 iterations. These parameter values are in agreement with those used before in the literature. Pixels were then selected using the "*L*-dimensional visualization tool"[15] in two different ways: 1) by selecting a set of $p = 20$ groups or clusters in *L*-dimensional space and then calculating the mean spectra of each resulting group; and 2) by selecting only $p = 20$ extreme pixels in the input data as the final set of endmembers. In order to determine appropriate parameters for IEA, we tested the algorithm using parameter values in the following intervals: $R = [10, 100]$ pixels, and $\theta = [0.01, 0.5]$. In general terms, we observed that the algorithm was not very sensitive to the setting of those parameters. In fact, even if the parameters R and θ were changed, within rather liberal limits, essentially the same endmembers were obtained. After several experiments, we set $R = 20$ and $\theta = 0.05$ in experiments for using the IEA algorithm as an EGA, and $R = 1$ and $\theta = 0$ for extracting $p = 20$ single pixel vectors and obtaining a traditional EEA-based funcionality from the algorithm.

As for the other considered methods, a previous performance study of our AMEE algorithm[9] revealed that satisfactory results can be obtained for this particular scene by setting K to a disk-shaped kernels of 7-pixel radius. This is mainly due

to the width in pixels of patterns of interest in the scene, and to the isotropic properties of disk structuring elements in mathematical morphology[14]. For similar reasons, the parameter $t^{(\mathrm{AMEE})}$ was set to its corresponding value of 0.05. As for the N-FINDR method, it should be noted that our implementation of this algorithm only requires as input parameter the number of endmembers to be extracted by the algorithm, which was set in this work to $p = 20$ for all methods after our estimation of the virtual dimensionality using the HFC method in Table 2. Finally, we must also point out that the developers of the ORASIS method at NRL optimized the algorithm's execution on the AVIRIS JRBP scene using their own parameter settings, which are unknown to us. However, in order to assess the impact of parameter $t^{(\mathrm{ORASIS})}$ on the quality of the exemplars selected by the algorithm, we conducted a simple experiment in which we set the value of $t^{(\mathrm{ORASIS})}$ to a range of values $t^{(\mathrm{ORASIS})} = [0.02, 0.03, 0.04, 0.05, 0.1, 0.2, 0.3, 0.5]$ and used the spectral similarity matching algorithm (SSMA) in Table 3 to establish the similarity between exemplar pixel vectors selected by our own implementation of the exemplar selection module in ORASIS, and the final endmember signatures generated by the algorithm after the minimum volume-based transformation. As shown in Table 3, the inputs to SSMA are $\Gamma_p = \{\boldsymbol{e}_i\}_{i=1}^{p}$, a set of p candidate endmembers, and $\Gamma_r = \{\boldsymbol{s}_j\}_{j=1}^{r}$, a set of r reference signatures (in our experiments, $p = 20$ and $r = 5$). The output of SSMA is a new set, Φ_r, which contains those endmembers in Γ_p that have been matched to available reference signatures according to a spectral similarity criterion.

Inputs: Γ_p, Γ_r.
Output: Φ_r.

Let $\Phi_r = \varnothing$
For i = 1 to p label $\boldsymbol{e}_i$ as "not matched"
For j = 1 to r do begin
    Min = ∞
    k = 0
    For i = 1 to p do begin
        If $\boldsymbol{e}_i$ is labeled as "not matched" then begin
            If $\mathrm{SAD}(\boldsymbol{e}_i, \boldsymbol{r}_j) < \mathrm{Min}$ then begin
                Min = $\mathrm{SAD}(\boldsymbol{e}_i, \boldsymbol{r}_j)$
                k = i
            Endif
        Endif
    Endfor
    If k > 0 then begin
        Label $\boldsymbol{e}_k$ as "matched"
        $\boldsymbol{m}_j = \boldsymbol{e}_k$
        $\Phi_r = \Phi_r \cup \boldsymbol{m}_j$
    Endif
Endfor

Table 3. Spectral similarity matching algorithm (SSMA).

Table 4 shows the spectral angle-based similarity scores between each exemplar selected by SSMA and its corresponding ORASIS-generated signature, labeled as $\{\boldsymbol{o}_i\}_{i=1}^{20}$, where values closer to 0 indicate highest similarity. Interestingly, the scores reported on Table 4 indicate that some of the final endmembers generated by ORASIS show little spectral similarity with regards to exemplars, even in the case where the threshold angle $t^{(\mathrm{ORASIS})}$ was set to 0.02, in which a very high fraction of the original image pixels were selected as exemplars. Further, results in Table 4 point out to the importance of carefully setting parameter $t^{(\mathrm{ORASIS})}$ in order to obtain the desired performance from the algorithm.

$t^{(\text{ORASIS})}$	o_1	o_2	o_3	o_4	o_5	o_6	o_7	o_8	o_9	o_{10}
0.02	0.055	0.034	0.068	0.105	0.070	0.027	0.029	0.051	0.047	0.060
0.03	0.056	0.035	0.068	0.101	0.070	0.027	0.029	0.050	0.047	0.061
0.04	0.055	0.036	0.068	0.101	0.070	0.027	0.029	0.050	0.047	0.061
0.05	0.055	0.035	0.068	0.101	0.069	0.028	0.028	0.050	0.047	0.061
0.1	0.059	0.039	0.041	0.101	0.060	0.027	0.029	0.029	0.048	0.063
0.2	0.068	0.039	0.041	0.112	0.060	0.032	0.029	0.029	0.049	0.063
0.3	0.069	0.042	0.053	0.112	0.065	0.033	0.029	0.027	0.050	0.066
0.5	0.076	0.037	0.071	0.112	0.078	0.037	0.035	0.058	0.051	0.062
$t^{(\text{ORASIS})}$	o_{11}	o_{12}	o_{13}	o_{14}	o_{15}	o_{16}	o_{17}	o_{18}	o_{19}	o_{20}
0.02	0.094	0.021	0.025	0.112	0.031	0.029	0.076	0.045	0.073	0.037
0.03	0.095	0.021	0.024	0.113	0.031	0.028	0.076	0.044	0.073	0.032
0.04	0.096	0.021	0.024	0.114	0.031	0.029	0.076	0.042	0.074	0.037
0.05	0.095	0.021	0.025	0.112	0.031	0.028	0.076	0.042	0.073	0.037
0.1	0.079	0.021	0.024	0.123	0.033	0.030	0.077	0.045	0.055	0.037
0.2	0.079	0.024	0.029	0.131	0.038	0.032	0.087	0.045	0.055	0.042
0.3	0.080	0.025	0.030	0.132	0.039	0.032	0.087	0.045	0.056	0.042
0.5	0.106	0.029	0.032	0.134	0.043	0.032	0.088	0.049	0.084	0.045

Table 4. Spectral angle-based similarity scores between exemplar pixel vectors and ORASIS-generated endmembers

Finally, Table 5 shows a cross-validation of the five methods in section 2 (with PPI and IEA implemented to work both as EEAs and EGAs) using ground-truth endmembers in Fig. 1(right) as reference signatures, indicating, for each case, whether the algorithm was used in endmember extraction-mode or endmember generation-mode. In all cases, the SSMA algorithm was run to find the 5 signatures (out of the 20 spectral signatures provided by each method) which resulted in the best match with regards to each of the reference signatures used for validation purposes.

Method	o_1	o_2	o_3	o_4	o_5
ORASIS (generation)	0.032	0.021	0.025	0.017	0.020
AMEE (generation)	0.009	0.007	0.008	0.006	0.018
N-FINDR (extraction)	0.028	0.025	0.022	0.020	0.019
PPI (extraction)	0.027	0.022	0.021	0.019	0.017
PPI (generation)	0.030	0.026	0.024	0.031	0.019
IEA (EEA)	0.018	0.015	0.019	0.012	0.014
IEA (EGA)	0.016	0.013	0.015	0.008	0.009

Table 5. Spectral angle-based similarity scores between the final endmembers provided by different algorithms and ground-truth endmember signatures in Fig. 1(right).

As shown by Table 5, the similarity scores achieved by ORASIS-generated signatures were significantly better than those reported on Table 4. This confirms our introspection that the exemplar selector module implemented in the algorithm acts only as a preliminary stage (pre-processing). Therefore, it was clear that the algorithm (in particular, the minimum volume transform algorithm) has the potential to recover from the initial condition given by exemplar vectors, and finally provide highly satisfactory results in terms of the quality of the spectral signatures, even though the initial exemplar selection of real pixel vectors may provide not completely pure exemplars in spectral terms. Overall, we observed that those algorithms able to work in both endmember extraction- and endmember generation-mode (i.e., PPI and IEA) provided similar results in experiments. This fact reveals that, even though both algorithm can indeed be used as EGAs through the averaging of clusters of endmembers in spectral space, the true fact is that both methods were originally conceived as EEAs and exclusively make use of real pixel vectors to generate new signatures through a straightforward averaging of results. Generally, the IEA showed better performance than PPI, in particular, when the two algorithms were used in generation-mode, which seems to indicate that manual selection of clusters in the PPI algorithm may result in cases where pixels that belong to slightly different spectral classes are incorrectly grouped together due to the manual interaction of the user. As for the AMEE algorithm, Table 5 shows that it generally showed good results for those endmembers that appear distributed in the form of homogeneous regions (e.g., soil) due to the spatial/spectral

integration accomplished by the algorithm, but showed poorer results with endmembers which do not seem to appear spatially correlated in the AVIRIS scene (e.g., the shade endmember). Finally, it is worth noting that the N-FINDR algorithm also provided accurate results in terms of spectral similarity. This fact demonstrates that image-derived endmembers also have the potential to represent pure signatures when dealing with images containing large and homogeneous areas, in particular, when the spatial resolution available does not represent a major obstacle to find pixel vectors with relatively high quality in terms of signature purity. Further work is still needed in order to assess the above remarks in more complicated analysis scenarios, i.e., using satellite data sets dominated by mixed pixels due to low spatial resolution and/or more significant multiple scattering effects than those observed in the application under study.

To conclude this paper, we must also point out that the lack of ground-truth information on fractional abundances of endmember materials prevented us from carrying out a detailed study on the impact of endmember quality on the final abundance estimation results that can be obtained by using standard linear/nonlinear SMA techniques. However, we conducted a simple experiment from a qualitative point of view. Such experiment was simply based on analyzing the fraction of negative and/or unrealistic abundance estimation values after applying an unconstrained linear spectral unmixing (ULSU)[3] approach, based on the endmembers provided by the different methods. For comparative purposes, we also applied a fully constrained (with abundance sum-to-one and non-negativity constrained) linear spectral unmixing (FCLSU)[8] approach. Our qualitative experiments demonstrated that the correspondent endmember fractional abundance maps, derived by using both FCLSU and ULSU, were in visual agreement for all the methods tested, in particular, for the two considered EGAs: ORASIS and AMEE. In addition, negative and/or unrealistic ULSU-derived abundance fractions, which usually indicate a bad fit of the model and reveal inappropriate endmember selections, were very rarely found, in particular when either ORASIS or AMEE were applied, while the number of such unrealistic fractions slightly increased when other algorithms were used in endmember extraction-mode. Having those results in mind, results obtained in this paper seem to indicate that generation of endmembers represents an alternative to endmember extraction, which may result in high-quality endmembers from the viewpoint of both signature purity and fractional abundance estimation.

5. CONCLUSIONS AND FUTURE RESEARCH

In this paper, we have examined endmember finding algorithms in terms of their capacity to derive spectral endmembers by selecting real pixel vectors, i.e., those available in the input data, or by generating artificial pixel vectors which are not present in the data to be analyzed. Such a distinction between a "real" and an "artificial" endmember has often been made from the viewpoint of whether the signatures provided by an algorithm can be associated to a spectral library of ground constituents, and taking into account the viability of relating such library spectra (collected under much different acquisition conditions) to image pixel vectors. To address this issue, we established a clear distinction between an endmember extraction algorithm (EEA), which finds pure pixels in the input data, and an endmember generation algorithm (EGA) which generates new signatures (not necessarily pixel vectors) with the purpose of obtaining better endmembers in terms of signature purity. Experimental results in this paper, obtained after a thorough comparison and cross-validation of five standard endmember extraction algorithms (two of which can behave both as EEAs and EGAs) revealed many interesting findings. In particular, we showed that endmember generation may constitute a valid and interesting alternative to endmember extraction when the goal is to find a compromise between the quality of the spectral signatures and their capacity to provide robust abundance estimations. Although experiments in this work were limited to a single AVIRIS data set and further experimentation is clearly needed to fully validate our preliminary conclusions in this work, we believe that endmember generation represents the future of this research area. In particular, although the spatial and spectral resolution of imaging spectrometers is ever increasing, the spatial requirements of certain applications in terms of the area to be covered (e.g., satellite imaging), are also increasing. Therefore, the possibility of using very high spectral resolution data to overcome the limitations introduced by the pixel size represents one of the most appealing solutions to produce fast and accurate analysis results with sub-pixel precision, for relatively large areas. Although experimental results addressed in this paper are preliminary, they point out to the future use of EGAs as a viable alternative to overcome the limitations introduced by the fact that most pixels in hyperspectral imaging applications are characterized by their mixed nature. We believe that this is an interesting remark, because such a distinction between EGAs and EEAs has been very rarely made before in the literature.

ACKNOWLEDGEMENT

We gratefully thank Drs. David Gillis and Jeffrey Bowles for their results and input on NRL's ORASIS algorithm.

REFERENCES

1. R. A. Schowengerdt, *Remote sensing: Models and methods for image processing, 2nd. Ed.*, Academic Press, 1997.
2. D. A. Landgrebe, *Signal theory methods in multispectral remote sensing*, Wiley: Hoboken, NJ, 2003.
3. C.-I Chang, *Hyperspectral imaging: Techniques for spectral detection and classification*, Kluwer Academic/Plenum Publishers: New York, 2003.
4. A. Plaza, P. Martínez, R. Pérez and J. Plaza, "A Quantitative and comparative analysis of endmember extraction algorithms from hyperspectral data," *IEEE Transactions on Geoscience and Remote Sensing*, vol. 42, no 2, pp.650-663, March 2004.
5. J. Bowles, D. Gillis, and P. Palmadesso, "New improvements in the ORASIS algorithm," in *Proc. IEEE Aerospace Conference*, Big Sky, MT, 2000.
6. M.D. Craig, "Minimum-volume transforms for remotely sensed data," *IEEE Transactions on Geoscience and Remote Sensing*, vol. 32, no 3, pp. 542-552, May 1994.
7. M.E. Winter, "N-FINDR: an algorithm for fast autonomous spectral endmember determination in hyperspectral data," *Image Spectrometry V*, *Proc. SPIE* 3753, pp. 266-277, 1999.
8. D. Heinz and C.-I Chang, "Fully constrained least squares linear mixture analysis for material quantification in hyperspectral imagery," *IEEE Transactions on Geoscience and Remote Sensing*, vol. 39, no. 3, pp. 529-545, March 2001.
9. A. Plaza, P. Martinez, R. Perez and J. Plaza, "Spatial/spectral endmember extraction by multidimensional morphological operations," *IEEE Transactions on Geoscience and Remote Sensing*, vol. 40, no 9, pp. 2025-2041, September 2002.
10. J. W. Boardman, F. A. Kruse and R. O. Green, "Mapping target signatures via partial unmixing of AVIRIS data," *Summaries of JPL Airborne Earth Science Workshop*, Pasadena, CA, 1995.
11. R.A. Neville, K. Staenz, T. Szeredi, J. Lefebvre and P. Hauff, "Automatic endmember extraction from hyperspectral data for mineral exploration," *4th International Airborne Remote Sensing Conf. and Exhibition/21st Canadian Symposium on Remote Sensing*, Ottawa, Ontario, Canada, pp. 21-24, June 1999.
12. R.O. Green et al., "Imaging spectroscopy and the airborne visible/infrared imaging spectrometer (AVIRIS)," *Remote Sening of Environment*, vol. 65, pp. 227–248, 1998.
13. A. Plaza, P. Martínez, R. Pérez, J. Plaza, "A new approach to mixed pixel classification of hyperspectral imagery based on extended morphological profiles," *Pattern Recognition*, vol 37, pp. 1097-1116, Jun. 2004.
14. A. Plaza, P. Martínez, J. Plaza and R. Pérez, "Dimensionality reduction and classification of hyperspectral image data using sequences of extended morphological transformations," *IEEE Transactions on Geoscience and Remote Sensing*, vol. 43, no. 3, pp. 466-479, 2005.
15. *Research Systems, Inc., ENVI User's Guide*. Boulder, CO: Research Systems, Inc., 2001.
16. M. García and S. L. Ustin, "Detection of interannual vegetation responses to climatic variability using AVIRIS data in a coastal savanna in California," *IEEE Transactions on Geoscience and Remote Sensing*, vol. 39, no. 7, pp. 1480-1490, 2001.
17. J. Plaza, A. Plaza, P.Martínez and R. Pérez, "H-COMP: A tool for quantitative and comparative analysis of endmember identification algorithms," *IEEE International Geoscience and Remote Sensing Symposium*, Toulouse, France, 2003.
18. C.-I Chang and Q. Du, "Estimation of number of spectrally distinct signal sources in hyperspectral imagery," *IEEE Transactions on Geoscience and Remote Sensing*, vol. 42, no. 3, pp. 608-619, March 2004.